Chinese Chemical Letters 35 (2024) 108861

Contents lists available at ScienceDirect

Chinese Chemical Letters

journal homepage: www.elsevier.com/locate/cclet

Key progresses of MOE key laboratory of macromolecular synthesis and functionalization in 2022

Xumeng Deng, Kaihao Chen, Kai Pang, Xiaoting Liu, Minsong Gao, Jie Ren*, Guanwen Yang*, Guangpeng Wu*, Chengjian Zhang*, Xufeng Ni*, Peng Zhang*, Jian Ji*, Jianzhao Liu*, Zhengwei Mao*, Ziliang Wu*, Zhen Xu*, Haoke Zhang*, Hanying Li*

MOE Key Laboratory of Macromolecular Synthesis and Functionalization, International Research Center for X Polymers, Department of Polymer Science and Engineering, Zhejiang University, Hangzhou 310027, China

ARTICLE INFO

Article history:
Received 5 June 2023
Revised 16 July 2023
Accepted 26 July 2023
Available online 27 July 2023

Keywords:
Polymer
Catalyst
Biomaterial research
mRNA
Hydrogel
Graphene
Crystal

ABSTRACT

In 2022, The MOE Key Laboratory of Macromolecular Synthesis and Functionalization in Zhejiang University had achieved several important results. First, a series of well-defined dinuclear organoboron catalysts were developed to precisely control the enchainment of ether and carbonate segments during the copolymerization of CO_2 and epoxides. Second, polyester had been synthesized through cationic copolymerization of cyclic anhydride. Third, ring-opening polymerization of carbon dioxide based valerolactone had been achieved, revealing the prospect of 3-ethylidene-6-vinyltetrahydro-2*H*-pyran-2-one (EVL) in utilizing CO_2 and synthesizing functional polymers. Fourth, machine learning methods have been applied to biomaterial research, enabling high-throughput screening of functional biomaterial surfaces for implantable devices, and searching for potent antimicrobial peptides in whole combinatorial peptide libraries. Fifth, methods of characterization of biomacromolecule RNA transcription and manipulation of nucleoside modification were developed. Sixth, artificial enzymes-armed *Bifidobacterium Longum* probiotics were established to tune down gut inflammation. Seventh, three-dimensional (3D) printing technologies were used to engineer tough supramolecular hydrogels. Eighth, hydroplastic foaming graphene frameworks for acoustic and conductive polymer composites were provided for application. Ninth, aggregate photophysics about the nature of through-space interactions (TSIs) and manipulating their strength in small molecules with non-conjugated structure had been elucidated. Tenth, the forming mechanism of a newfound nested texture in poly(L-lactic acid) (PLLA) spherulitic films had been revealed. Finally, the isotropically dyeing mechanism of KDP single crystals grown from hydrogels have been explored. The related works are reviewed in this paper.

1. Introduction

The MOE Key Laboratory of Macromolecular Synthesis and Functionalization, set up in 2005, focus on the fundamental and applied polymer science, which include controllable catalytic polymerization, microstructure and rheology, photo-electro-magnetic functional polymers, biomedical functional polymers and separating functional polymers [1,2]. Focusing on the development frontier of polymer science at home and abroad, the laboratory has been built into a key laboratory combining science and technology, interdisciplinary, facing the needs of energy information, human health, environmental resources and other aspects, leading the domestic level and having certain international academic influence. The laboratory seeks breakthroughs in five research directions: controlled catalytic polymerization, microstructure and rheology, photoelectromagnetic functional polymers, biomedical functional polymers and separation functional polymers.

In 2022, the laboratory has obtained abundant research achievements in the aforementioned five research directions, which are worth emphasizing. Next, we intend to review some of the leading research results published in 2022. Publications of eleven research areas are selected, including organoboron catalysts, polyester synthesis, ring-opening polymerization, biomaterial research, characterization of biomacromolecule RNA transcription

* Corresponding authors.
E-mail addresses: jie.ren@zju.edu.cn (J. Ren), yangguanwen@zju.edu.cn (G. Yang), gpwu@zju.edu.cn (G. Wu), chengjian.zhang@zju.edu.cn (C. Zhang), xufengni@zju.edu.cn (X. Ni), zhangp7@zju.edu.cn (P. Zhang), jijian@zju.edu.cn (J. Ji), liujz@zju.edu.cn (J. Liu), zwmao@zju.edu.cn (Z. Mao), wuziliang@zju.edu.cn (Z. Wu), zhenxu@zju.edu.cn (Z. Xu), zhanghaoke@zju.edu.cn (H. Zhang), hanying_li@zju.edu.cn (H. Li).

https://doi.org/10.1016/j.cclet.2023.108861
1001-8417/

and manipulation of nucleoside modification, artificial enzymes-armed *Bifidobacterium Longum* probiotics, 3D printing of tough supramolecular hydrogels, hydroplastic foaming graphene frameworks, aggregate photophysics, polymorphic texture of polymer spherulites and single crystal dyeing.

2. The developments and catalytic performances of organoboron catalysts

Copolymerization of CO_2 and epoxides is an industrially relevant method to alleviate anthropogenic carbon emissions and produce reproducible plastics [3]. Despite recent advances, few studies have focused on enchainment control during the copolymerization process, which can ultimately determine the performance of the resultant materials [4–6]. Among the underdeveloped research directions, the precise control of the enchainment of ether and carbonate segments, and the sequence-controlled polymerization from epoxide congeners has never been realized.

Bearing this in mind, we developed a suite of well-defined dinuclear organoboron catalysts for the copolymerization of CO_2 and epoxides with an aim to achieve enchainment control (Figs. 1a and b) [7]. By altering the catalyst structure and optimizing reaction conditions, the alternating carbonate content in the propylene oxide/CO_2 copolymer was finely regulated over a wide range of 3.0%–95.2%, and the polyether content was arbitrarily varied between <0.1% and 97.0% (Fig. 1a). Of great interest, an unprecedented double insertion of propylene oxide in the copolymer was observed, affording a -ABB- linkage, which was identified by NMR spectroscopy, hydrolysis-derivatization experiments and single-crystal X-ray diffraction. A relationship between catalyst structure and catalytic performance was then revealed by systematic tuning catalyst structure. Density functional theory calculations indicate that the -ABB- microstructure originates from a regioselectivity-directed copolymerization process. More specifically, the selectivity of the alternating -AB-, novel -ABB- and etheric -AB_n- linkages showed linear correlations with boron···boron distances [5].

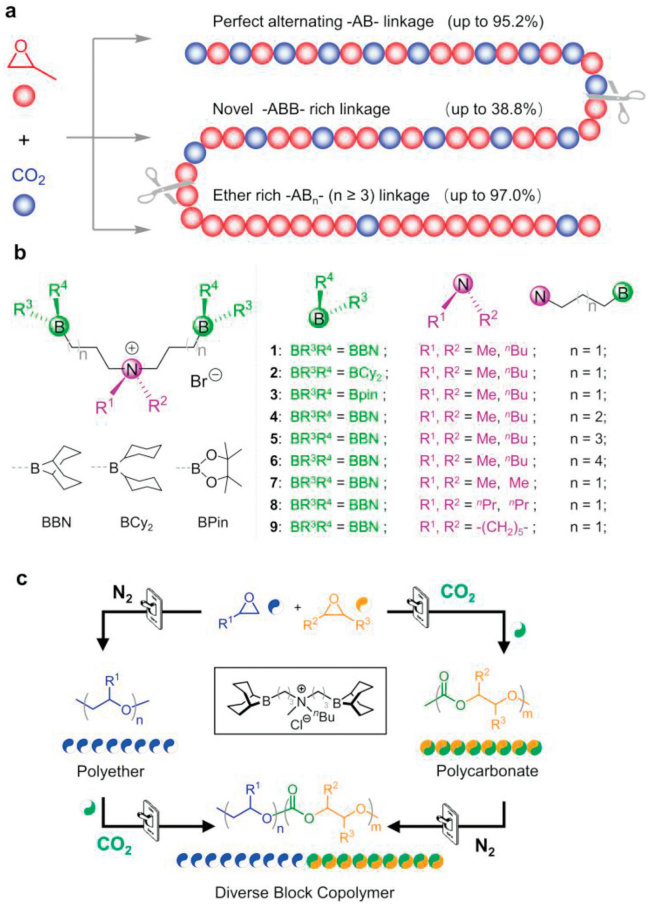

Fig. 1. (a) Sequence control in copolymerization of propylene oxide and CO_2. Polymers with different contents of -AB-, -ABB- and -ABn- ($n \geq 3$) linkages can be obtained by adjusting catalyst structure and reaction conditions. (b) The modularly designed dinuclear organoboron catalysts used for the copolymerization of propylene oxide and CO_2. Cy, cyclohexyl; BPin, 4,4,5,5-tetramethyl-1,2,2-dioxoboryl. Reproduced with permission [7]. Copyright 2022, Springer Nature. (c) Sequence-controlled polymerization of epoxide mixtures mediated by N_2 and CO_2 atmospheres. Reproduced with permission [8]. Copyright 2022, American Chemical Society.

We also demonstrated that, for the first time, well-defined polyether-*block*-polycarbonate copolymers could be obtained in a switchable manner from epoxide congeners by using our dinuclear catalysts [8]. Specifically, the catalyst selectively polymerizes terminal epoxide to afford the polyether block under N_2 atmosphere; by applying CO_2, the catalytic process switches to the ring-opening copolymerization of CO_2 and internal epoxide (Fig. 1c). The construction of polyether-*block*-polycarbonate copolymers was confirmed by NMR, MALDI-TOF, and GPC analyses. Kinetic studies and density functional theory calculations elucidated the reversible selectivity between different epoxides in the presence/absence of CO_2. Moreover, by replacing comonomer CO_2 with cyclic anhydride, the well-defined polyether-*block*-polyester copolymers can also be synthesized [8].

In addition to the above-mentioned progresses regarding our bifunctional organoborane catalysts, we also communicated a superior organoboron system by replacing a nitrogen atom with a phosphorus atom. The upgraded mono-, di-, and trinuclear organoboron catalysts show significantly improved catalytic performance and heat resistance for versatile epoxide-involved transformations, including ring-opening copolymerization of epoxides and cyclic anhydrides, copolymerization of CO_2 and epoxides, and ring-opening polymerization of epoxides [9]. We also found that the increase of Lewis acidity and the number of B centers of the organoboron catalysts are useful for a high catalytic activity for ROP of epoxides, and the Lewis acidity of the B centers was determined using the acceptor numbers, showing an order of borinane (23.4) > BBN (21.7) > BCy_2 (18.8) > Bpin (15.5) [10]. By using the dinuclear bifunctional organoboron catalysts, the first metal-free access to poly(cyclopentene carbonate) and its chemical recycling to monomer was also achieved in 2022 in our laboratory [11].

In summary, we developed a series of well-defined dinuclear organoboron catalysts to precisely control the enchainment of ether and carbonate segments during the copolymerization of CO_2 and epoxides, and selectively polymerize a specific epoxide from epoxide mixtures. We deemed that the facile approach to precise CO_2-based copolymers will be of value to next-generation materials.

3. Polyester synthesis through cationic copolymerization of cyclic anhydride

Aliphatic polyesters have been regarded as a sustainable alternative to petroleum-based polyolefins because of abundant renewable feedstocks, biocompatibility, and biodegradability [12–15]. The development of facile and versatile methods to synthesize novel polyesters is highly desired, but remains challenging. The alternating copolymerization of epoxide and cyclic anhydride is a widely studied atom-economical and chain-growth method for the synthesis of aliphatic polyesters [16–18]. Advances have enabled the method to produce diverse polyesters from two distinct monomers [19,20]. In the copolymerization method with a coordination/anionic mechanism, three-membered epoxides have a

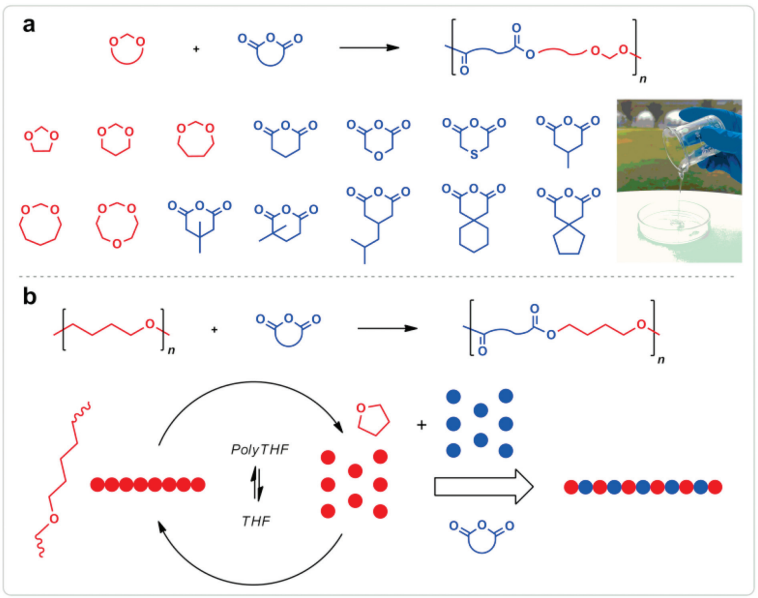

Fig. 2. Polyester synthesis from cyclic anhydrides. (a) Alternating copolymerization of cyclic acetal and anhydride to yield various polyesters. Reproduced with permission [21]. Copyright 2022, Wiley-VCH. (b) One-step upcycling of PTHF to polyesters using cyclic acetal anhydride as a monomer. Reproduced with permission [22]. Copyright 2023, licensed under CC-BY.

high tension that enables them with high reactivity during their copolymerization. However, the coordination/anionic copolymerization of cyclic anhydride and low-tension heterocyclic compound has rarely been achieved. Analyzing the possible reasons, the oxygen anion active species is too weak to attack the carbon atoms with weaker polarity. According to this inference, the alternating copolymerization of cyclic anhydride and low-tension heterocyclic is possible to achieve with a cationic mechanism.

We reported the alternating copolymerization of cyclic acetal and anhydride with a cationic mechanism (Fig. 2a) for the first time [21]. The method used 5 cyclic acetals and 9 cyclic anhydrides to synthesize 45 polyesters with the unprecedented structure. A variety of common and metal-free Lewis/Brønsted acids were used as effective catalysts for the copolymerization at the wide reaction temperatures from 25 °C to 140 °C. According to kinetic studies, the alternating copolymerization shifted the chemical equilibrium of "poly(acetal) ⇌ cyclic acetal" to the left, affording polyesters with the alternating sequence. The produced polyesters possess a high oxygen content, M_n of 2.0∼33.3 kDa, $Đ$ of 1.2∼1.5, high decomposition temperatures (275∼324 °C), and low glass transition temperatures (−64∼−27 °C). The study provides a facile approach for preparing diverse oxygen-rich and thermally stable polyesters using readily available chemicals.

Based on the cationic mechanism for cyclic anhydride copolymerization, we reported a "polymer A → polymer B" strategy for one-step quantitative upcycle of polytetrahydrofuran (PTHF) to polyesters using cyclic anhydride as a monomer (Fig. 2b) [22]. PTHF is widely used in the production of thermoplastic polyurethane and polyetherester elastomers, but it is difficult to chemically reuse after disposal owing to the stable ether bonds. In our strategy, PTHF is firstly depolymerized to yield THF that is then copolymerized with cyclic anhydrides, thus driving the equilibrium of "PTHF ⇌ THF" to the right. The method used common Brønsted/Lewis acids as catalysts, was carried out at 100 °C and solvent-free. The approach also used 18 cyclic anhydrides to yield 18 polyesters with alternating sequence and carboxyl terminals. This strategy provides a new idea for chemical recycling of waste PTHF.

4. Ring-opening polymerization of carbon dioxide based valerolactone

Following the worldwide trend in developing green, low-carbon and circular economy, the utilization of carbon dioxide (CO_2) has attracted increasing attentions [23–26]. The copolymerization of CO_2 and alkenes, inexpensive bulk chemicals in petroleum-based industry, is a cost-competitive approach to achieve the carbon neutrality goal and produce valuable polymers. Nonetheless, the challenge of the direct copolymerization has been revealed with both experimental and computational evidences [27,28]. As a product of the telomerization of CO_2 and 1,3-butadiene, the di-substituted valerolactone 3-ethylidene-6-vinyltetrahydro-2*H*-pyran-2-one (EVL) is a promising candidate to bypass the energy barrier of the direct copolymerization [29]. With two C=C double bonds and a lactone ring, EVL was applicated as a vinyl monomer in the synthesis of various functional polymers in the past decade, while polyesters were never obtained until our first report in 2021 due to its inertness in ring-opening polymerization [30–32]. We recognize that the EVL oligomer (oEVL) generated from a base catalyzed addition oligomerization contains three kinds of lactone rings, of which the unconjugated one is the activated and most active one, on the basis of density functional theory (DFT) calculation results (Fig. 3a) [33]. Accordingly, a novel strategy named "scrambling polymerizations" is performed to prepare topology-defined polyesters from EVL and ε-caprolactone (CL) (Fig. 3b). In the presence of sodium phenolate (NaOAr), an economic and nontoxic catalyst, EVL and CL firstly undergo addition oligomerization and rapid ring-opening polymerization respectively, resulting in oEVL and PCL. As the DFT calculation results revealed, the energy barrier of transesterification between oEVL and PCL is as low as 4.3 kcal/mol, far lower than the one of oEVL propagation (8.0 kcal/mol). The frequent transesterification between oEVL and PCL gradually yield cyclic (as major) copolymers with increasing EVL contents (Fig. 3c), which can reach a maximum of 50 mol%. Then, the activated lactone ring in the middle of oEVL takes part in the intermolecular transesterification, generating copolymers with branched and cross-linked topologies. The cross-linked polyester network has great cell

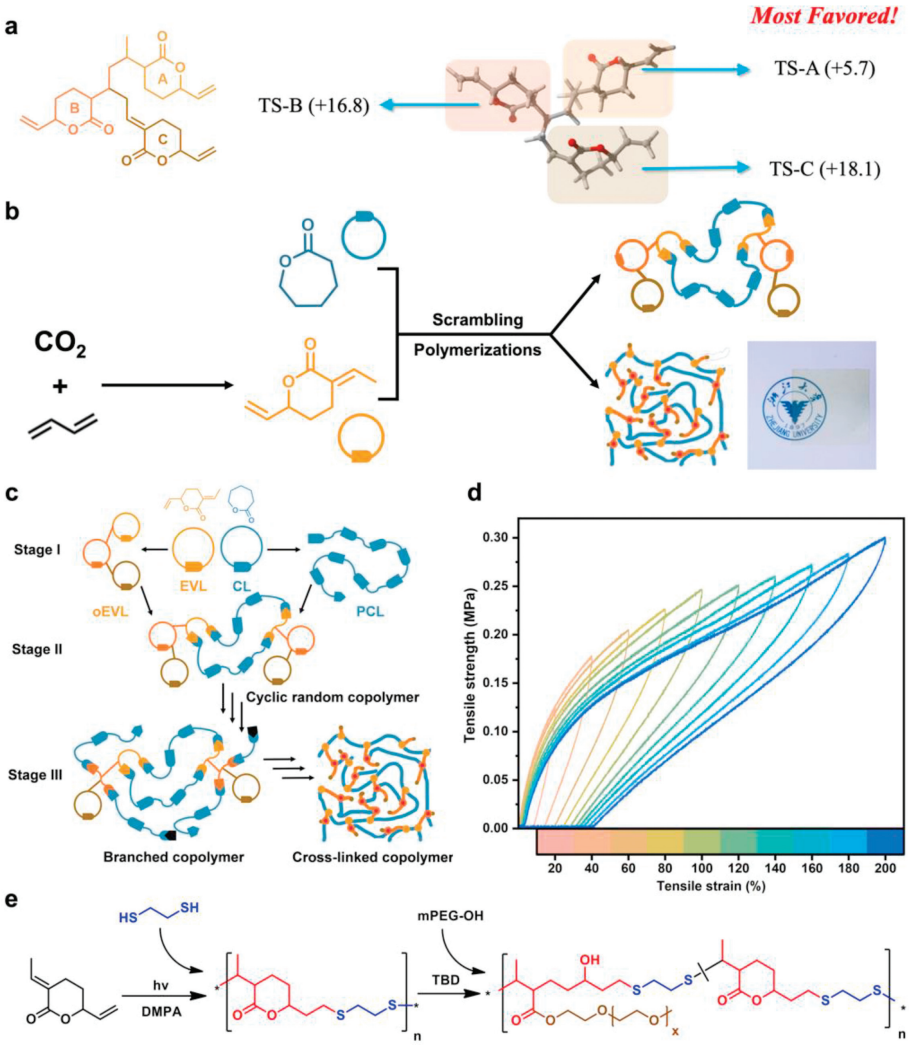

Fig. 3. (a) Chemical structure and DFT-optimized 3D structure of the trimer of EVL as well as Gibbs free energy barriers of transition states (TS) of carbonyl addition step on each ring in the trimer of EVL (kcal/mol). (b) Scheme of "scrambling polymerizations". (c) Scheme of three stages in "scrambling polymerizations". (d) Step-cyclic uniaxial tensile stress-strain curve of the cross-linked copolymer specimen. Reproduced with permission [33]. Copyright 2022, Wiley-VCH. (e) Orthogonal thiol-ene click polymerization and ring-opening reaction of EVL, 1,2-ethylene dithiol and methoxy polyethylene glycol bearing one hydroxyl terminal group (mPEG-OH). DMPA: 2,2-dimethoxy-2-phenylacetophenone, TBD: 1,5,7-triazabicyclo[4.4.0]dec–5-ene. Reproduced with permission [34]. Copyright 2022, Wiley-VCH.

compatibility, tensile strength (>1.7 MPa), elongation at break (>700%) and repeatable elastic recovery, which enable its application in the elastomer field (Fig. 3d). On the other hand, the saturated lactone rings in the alternating copolymer synthesized from the thiol-ene "click" polymerization of EVL with 1,2-ethanedithiol can also be subjected to ring-opening reactions that orthogonal to the "click" polymerization (Fig. 3e) [34]. Polyethylene glycol is grafted onto the alternating copolymer to prepare amphiphilic polymer, whose self-assembled micelle in aqueous solution have an average hydrodynamic diameter of 98 nm. The above studies reveal the prospect of EVL in providing new methods to utilize CO_2 and synthesizing functional polymers.

5. Machine learning-assisted biomaterial research

In recent years, significant progress has been made in artificial intelligence (AI), particularly in machine learning [35,36]. These technologies have been utilized in material research to quickly screen, simulate and predict vast numbers of potential materials, resulting in faster design processes and reduced costs [37–40]. In a previous study, we developed a machine learning-based method using combinational models to identify endothelial cells (ECs) and smooth muscle cells (SMCs) in a co-culture system without the need for labeling [41]. This algorithm provided automatic identification and real-time statistics of co-cultured cells. Recently, we have integrated orthogonal gradient chips with the machine learning-based cellular analysis to build a high-throughput workflow for systematic study of the biological effects of surface co-grafted functional molecules [42]. Arginine-glutamic acid-aspartic acid-valine peptide (REDV) is a functional peptide that aids in the attachment of ECs. Further study revealed that the combination of grafting REDV with a nonfouling polymer polyethylene glycol (PEG) could improve the selective growth of ECs on the surface over SMCs by leveraging both nonspecific resistance and specific cell interaction [43]. Using the integrated setup, we studied the effects of the combinational densities of PEG and REDV on cell competitiveness in the EC/SMC co-culture and identified an optimal composition that induced the highest EC selectivity. We further validated the biological effects of the compositions found through the orthogonal gradients on independent large surfaces. Furthermore, we translated the optimal composition as a potential surface coating formula for implantable cardiovascular devices to facilitate re-endothelialisation. Our workflow provides an efficient way to study and screen the biological effects mediated by the

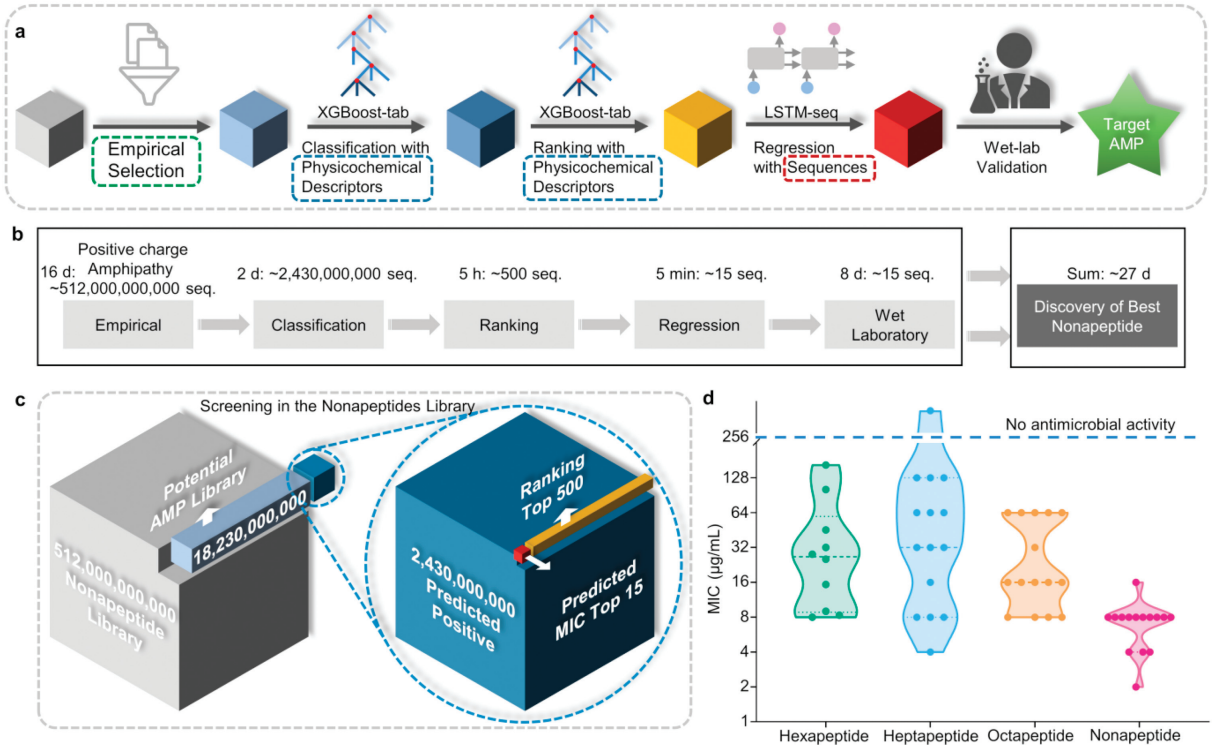

Fig. 4. (a) The whole process of SMEP includes modules of empirical selection, classification, ranking and regression enhanced by an incremental learning mechanism. The antimicrobial activities of the output peptide sequences were validated by wet-lab experiments. (b) Time spent in each step of the process for nonapeptides screening. (c) Reduction of the search space of nonapeptides step-by-step *via* the sequential assembly of the modules. (d) Antimicrobial activities of the top-predicted AMPs against *S. aureus* ($n = 3$ biologically independent replicates). The dashed line represents MIC = 256 μg/mL. The dotted lines in each data group represent the first quartile, median and third quartile. Reproduced with permission [48]. Copyright 2023, Springer Nature.

combinations of different surface-immobilized functional molecules in high-throughput settings.

In addition to AI-assisted image analysis, we also used machine learning methods to search for functional peptides. Peptide molecules are oligomers or polymers made up of amino acids. Because of the diversity of these amino acids, peptide sequences offer an immense potential for developing therapeutics [44]. For instance, a 10-mer peptide consisting of only the twenty standard proteinogenic amino acids possesses over one trillion distinct possibilities. Traditional peptide drug discovery relies on identifying functional peptides from nature, which limits the search space for drug candidates [44]. Antimicrobial peptides (AMP) show promise as a supplement to antibiotics to treat drug-resistant bacterial infections [45–47]. To identify high-performance AMPs, we developed an efficient and robust approach called the Sequential Model Ensemble Pipeline (SMEP) [48]. This approach involves multiple steps, including empirical selection, classification, ranking, regression, and wet-lab validation, as shown in Fig. 4. Theoretically, using a single machine learning model, one could screen and predict the antimicrobial activity of peptides drawn from the vast search space. However, this is not feasible in practice because the inductive bias of any individual model can pose problems when considering the limited training dataset and the numerous unseen testing examples. Therefore, our approach employs a set of models that sequentially narrow down the search space, supplemented by a model adjustment process *via* continuous learning. With SMEP, we identified a series of potent AMPs from the entire search space of hexa-, hepta-, octa-, and nona-peptide libraries within a short period. Through wet-lab validation, we confirmed the necessity of each step in the pipeline. The complete process gave the most accurate prediction results, which proved the rationality of our coarse-to-fine design principle. Notably, when testing the setup on the whole nonapeptide library, we identified, synthesized, and experimentally tested 15 candidates from the 512 billion sequences in the pool within 27 days, of which 14 displayed high potency against the tested pathogens. Our training dataset and model assembly development do not include any bias on peptide sequence length, meaning that theoretically, SMEP can easily apply to AMP screening at any length without model adjustments. Furthermore, when testing the leading hexa-AMPs, we found low off-target toxicity and strong antimicrobial activity against a collection of clinical-derived multidrug-resistant bacterial strains, including *A. baumannii*. These hexapeptides did not induce drug resistance in *S. aureus* after 100 generations of bacterial culture. Furthermore, aerosolized formulation of the leading peptides showed similar therapeutic efficacy and safety as the classic antibiotic penicillin in both healthy and bacterial pneumonia mouse models. Altogether, the hexapeptides uncovered in this study showed great potential as next-generation antibiotics, validating the effectiveness of the SMEP framework in screening peptide drugs across the entire combinatorial search space.

6. Development of methods for characterization of biomacromolecule RNA transcription and manipulation of nucleoside modification

Biomacromolecule messenger RNA (mRNA), with a role in transmitting genetic information, is strictly and sophistically regulated from initial transcription generation to eventual degradation [49–51]. As RNA polymerase II controls the transcription process of mRNA [49], precise localization of cellular RNA polymerase II genome-wide is essential for understanding the regulatory networks of gene expression. Currently, the main methods for mapping RNA polymerase II involve tedious procedures for immunoprecipitation and high complexity in library preparation, leading to high cost as well as low resolution or potential false positive

target detection [52]. In this regard, there is an urgent need to develop a simple, high-resolution and cost-effective method to meet the current needs for multiple omics characterization of scientific questions. mRNA nucleoside modifications occur in the co- or post-transcriptional processes, and they add a new layer to regulate gene expression. N^6-methyladenosine (m^6A) is the most abundant internal modification of mRNA, and exhibits significant biological functions in regulating mRNA splicing, nuclear export, translation, and stability [52–54]. The biological functions of m^6A are generally probed by modulating the cellular expression of m^6A methyltransferases or demethylases, which tune the global mRNA m^6A level, but are not able to manipulate the methylation extent at particular single site.

We have developed new simple and effective methods for mapping RNA polymerase II site at base resolution and for manipulating single-site m^6A methylation, in order to meet the increasing need for efficient and sophisticated characterizations of mRNA transcription and nucleoside modification (Fig. 5) [55,56]. First, we developed a mutation-based and enrichment-free Global chromatin Run-On sequencing (mGRO-seq) technique to precisely locate cellular RNA polymerase II sites genome-wide with base resolution (Fig. 5a) [55]. This method takes advantage of an ATP analog,

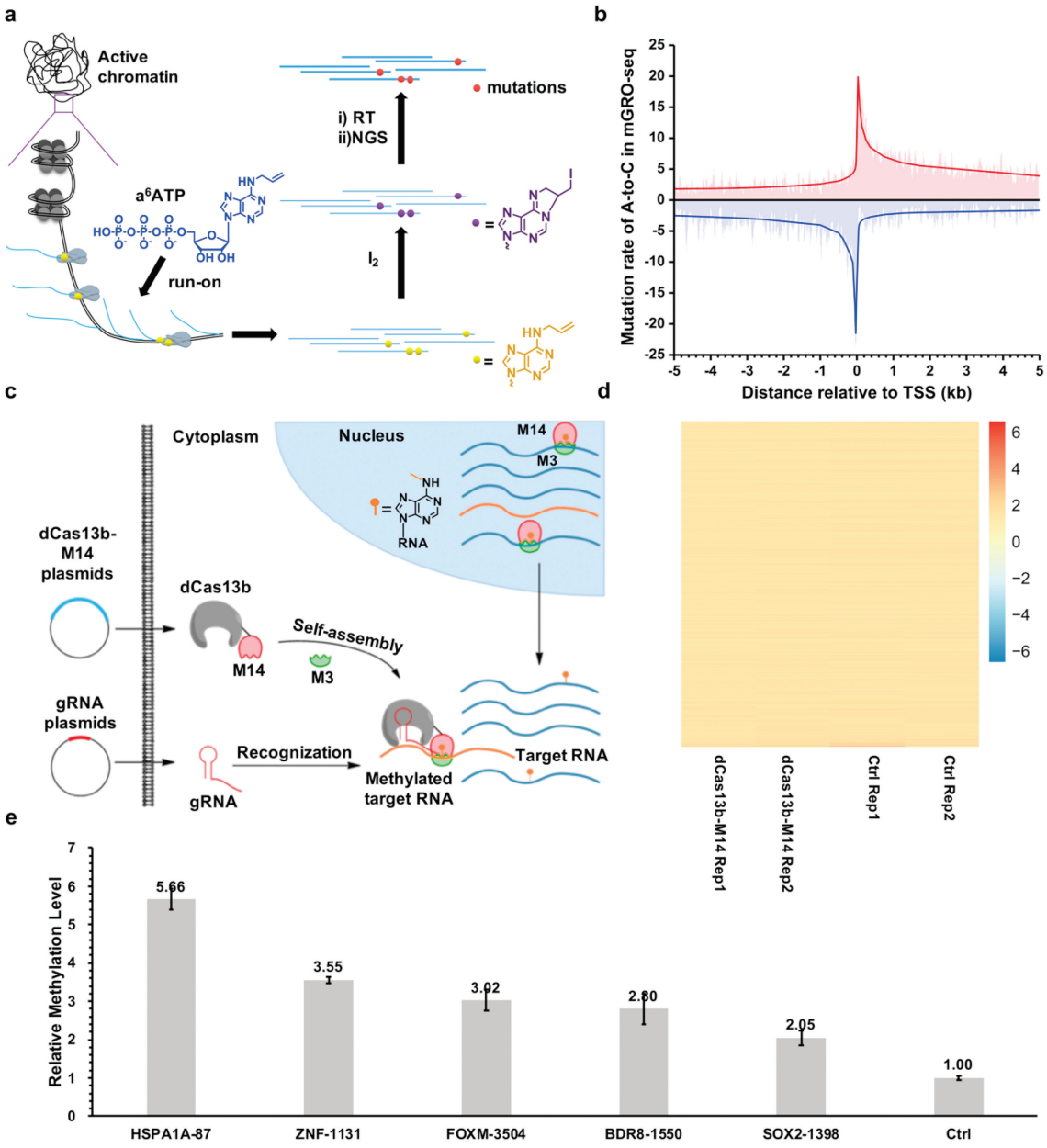

Fig. 5. (a) A schematic illustration of mutation-based global chromatin run-on sequencing (mGRO-seq) technique, which is enrichment-free and cost-effective in mapping RNA polymerase II sites with near base resolution. (b) The cumulative mutation rates in mGRO-seq around RefSeq TSS by 50 bp-windows. The signals in both sense and antisense directions relative to the direction of gene transcription were shown in red and blue, respectively. The solid lines were drawn for a clear indication of trends. (c) A schematic illustration of RNA N^6-methyladenosine editor. The RNA N^6-methyladenosine editor dCas13b-METTL14 (M14) is designed to be positioned in cytoplasm. Together with guide RNA (gRNA), dCas13b-M14/METTL3 (M3) heterodimer can be specifically recruited to a target RNA to perform site-specific methylation. (d) The *in vivo* off-target study of dCas13b-M14/gRNA system in HEK293T cells. A heatmap showing mRNA m^6A peak signal differences among the listed samples. (e) The *in vivo* results of dCas13b-M14/gRNA-mediated site-specific de novo m^6A methylation on the listed target sites. GAPDH was used as Ctrl. Reproduced with permission [55,56]. Copyright 2022, American Chemical Society.

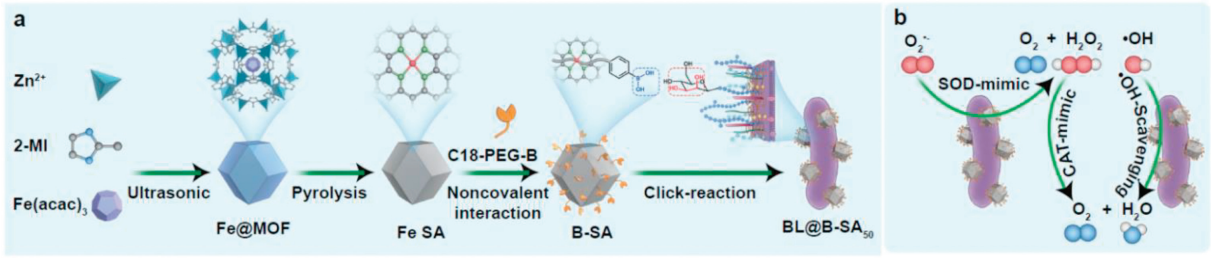

Fig. 6. Scheme of artificial-enzyme-armed probiotics. (a) BL@B-SA_{50} is composed of artificial enzymes (Fe SA), BL probiotics and linkers (C18–PEG-B) to conjugate them. Fe SA is fabricated through the pyrolysis of Fe@MOF. The linker C18–PEG-B comprises a hydrophobic C18 group that can be attached to the Fe SA surface through non-covalent interactions and a phenylboronic acid functional group to capture bacteria *via* a boronic acid vicinal-diol-based click reaction. (b) BL@B-SA_{50} can mimic SOD and CAT antioxidant enzymes as well as function as antioxidant molecules to scavenge multiple ROS to regulate the fate of cells and microbes. Reproduced with permission [69]. Copyright 2023, Springer Nature. BL: *Bifidobacterium Longum*.

namely N^6-allyladenosine triphosphate (a^6ATP) [57,58], to mark the site of RNA polymerase II in nascent RNA during a chromatin run-on reaction. After a^6A on the run-on RNAs is treated with a mild iodination reaction, base misincorporation is induced during RNA reverse transcription into the complementary DNA (cDNA), and thus the genome-wide RNA polymerase II locations could be detected in the high-throughput cDNA sequencing [55,57]. The cumulative mGRO-seq signals reveals strong and sharp peaks both in sense and antisense directions around the transcription start site (TSS), which are well consistent with the published results of divergent transcription (Fig. 5b) [59,60]. Also, we have developed a tool for precise manipulation of cellular mRNA m^6A methylation at base level [56]. A fusion protein containing deactivated nuclease Cas13b (dCas13b) and m^6A methyltransferase METTL14, namely dCas13b-METTL14, is designed to be positioned in cytoplasm. dCas13b-METTL14 naturally heterodimerizes with endogenous METTL3 to form a catalytic complex to methylate specific cytoplasmic mRNA in the presence of guide RNAs (gRNAs) (Fig. 5c). This tool exhibits a very minor and almost negligible off-target effect on whole transcriptome (Fig. 5d), and can successfully tune methylation levels of several selected mRNA m^6A sites (Fig. 5e). In summary, we have developed base-resolution methods to map cellular RNA polymerase II sites and to manipulate m^6A methylation. Due to the lower cost and higher accuracy, these methods will facilitate the in-depth study of mRNA transcription and nucleoside modifications and will promote the understanding of genetic information expression.

7. Artificial enzymes-armed *Bifidobacterium Longum* probiotics for alleviating intestinal inflammation and microbiota dysbiosis

Inflammatory bowel disease (IBD) can be caused by dysfunction of the intestinal mucosal barrier [61] and dysregulation of gut microbiota [62,63], and subsequently results in hyperactive immune responses of elevated reactive oxygen species (ROS) and inflammatory factors [64]. Traditional treatment uses drugs to manage inflammation with possible probiotic therapy as an adjuvant to positively modulate the balance of bacterial composition and promote intestinal mucosal repair [65,66]. However, current standard drug practices often suffer from metabolic instability, limited targeting and result in unsatisfactory therapeutic outcomes [67]. Additionally, due to the lack of antioxidant enzymes, such as catalase (CAT) and superoxide dismutase (SOD), these strictly anaerobic probiotics are susceptible to the ROS damage in IBDs [68], thus reducing the therapeutic effect and extending the treatment period. There is an unmet need for a more effective and safer treatment for IBD that can effectively target inflamed colon and rapidly reshape a sanatory immune microenvironment by suppressing the inflammation, remodeling the intestinal barrier function and modulating the gut microbiome in the infected tissues.

Herein, artificial enzymes-armed *Bifidobacterium Longum* probiotics have been established to tune down gut inflammation (Fig. 6) [69]. In this platform, the artificial enzymes of single-atom catalyst (SAzymes), a type of nanomaterial that contains atomically dispersed active metal centers, have been employed to efficiently mimic natural antioxidant defense systems to not only replace clinically used anti-inflammatory drugs but also shield commercial probiotics from hostile stressors. Specifically, they can mimic antioxidant enzymes of SOD and CAT to scavenge superoxide radical ($O_2^{\bullet-}$) and hydrogen peroxide (H_2O_2), and function as antioxidant biomolecules to eradicate hydroxyl radical ($^{\bullet}OH$), robustly and rapidly relieving the inflammatory symptoms [70]. Furthermore, they could also serve as the guardian of probiotics to protect these encased microbes from oxidative damage in the inflamed habitat, thus rapidly redirecting the barrier functions and gut microbiome towards a sanatory state. In addition, *Bifidobacterium Longum* probiotics, one common inhabitant, not only confer a health benefit on the host and but also possess superior intestinal colonization ability in the colon among probiotics [71], ensuring the persistent antioxidant therapy of SAzymes at the disease site. Thus, the SAzymes-armed probiotics BL@B-SA_{50} could reduce ROS levels, inhibit proinflammatory cytokine production, restore the intestinal barrier functions, and increase the richness and diversity of gut microbiota in murine models of ulcerative colitis (UC) and Crohn's disease (CD). Most importantly, in beagle dogs challenged with colitis, BL@B-SA_{50} also demonstrated prominent therapeutic potential, greatly accelerating the process of artificial enzymes-armed probiotics in clinical translation.

8. 3D printing of tough supramolecular hydrogels

Polymer hydrogels are a typical class of soft materials which consist of a physically or chemically crosslinked network and large amount of water. Hydrogels such as jellies are usually recognized to be mechanically weak, limiting their applications at load-bearing conditions. In the last two decades, various tough hydrogels have been developed by the designs of network structures and invoking of energy dissipation mechanisms, enabling hydrogels to be structural materials with versatile applications in biomedical and engineering fields [72–79]. For practical applications, it is highly desired to engineer tough hydrogels into sophisticated architectures. However, this topic receives much less attention, when compared to the rapid development of tough hydrogels. There are only a few attempts to process tough hydrogels by extrusion or compression molding at specific conditions [80,81], and the resulting structures/shapes of tough gels are relatively simple and have low resolution and fidelity. Three-dimensional (3D) printing is a powerful additive manufacturing technology to process materials into elaborate structures. Extrusion-based 3D printing has been applied to develop scaffolds for cell culture by using soft and weak

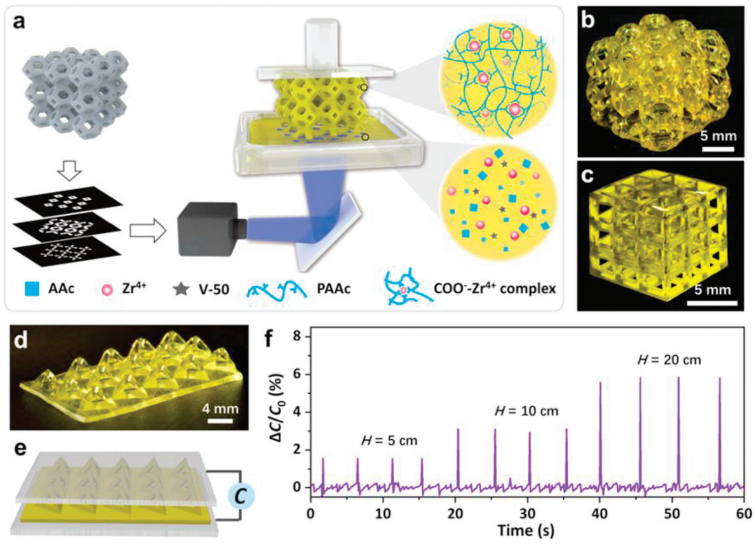

Fig. 7. (a) Schematic of DLP-based 3D printing of tough hydrogels by *in situ* formation of carboxyl-Zr^{4+} coordination complexes. Photos of printed gel architectures of Kelvin cell (b) and cubic lattice (c). Photo of printed gel film with hollow pyramid-like bulges on the surface (d), assembled capacitive pressure sensor with the printed gel sandwiched by a pair of conductive carbon fabric sheets (e), and real-time variations of relative capacitance $\Delta C/C_0$ of the pressure sensor to monitor the dripping of water droplets from different height H (f). Reproduced with permission [85]. Copyright 2022, Wiley-VCH.

hydrogels (*e.g.*, gelatin and alginate gels) as the ink [82,83]. Digital light processing (DLP) based 3D printing with "bottom-up" projection is only applicable to several systems (*e.g.*, poly(ethylene glycol) diacrylate), because most gels have relatively low stiffness and cannot resist the influence of gravity [84]. It is urgently desired yet highly challenging to realize printing of tough hydrogels into elaborate 3D architectures.

Recently, we reported a versatile system of tough supramolecular hydrogels suitable for DLP-based 3D printing to develop sophisticated architectures with tunable mechanical performances (Fig. 7a). The aqueous precursor solutions containing concentrated acrylic acid (AAc; 5 mol/L), commercial photo-initiator (2,2′-azobis(2-methylpropionamidine) dihydrochloride, V-50), and appropriate amount of Zr^{4+} ions can be rapidly polymerized to form tough supramolecular hydrogels when exposed to digital light [85]. During the DLP printing process, carboxyl groups of the reaction-produced poly(acrylic acid) (PAAc) form strong coordination complexes with the Zr^{4+} ions, leading to timely formation of tough metallosupramolecular hydrogels [86–89]. The gelation and toughening processes are fast, favoring the creation of 3D architectures of hydrogel with a high fidelity. The as-printed supramolecular hydrogels possess excellent mechanical properties and anti-swelling behavior in the precursor solution, enabling continuous DLP printing to develop tough gels with various architectures such as Kelvin cell and cubic lattice (Figs. 7b and c). When being swelled in water, the printed gels further increase their stiffness and toughness because of the increase in local pH and thus the rearrangement of coordination complexes [85,86].

The DLP-based printing of tough hydrogels is meaningful for the design of structural elements that are important for the assembly of soft devices or machines with versatile functions. As shown in Fig. 7d, structured surface with an array of hollow pyramid-like bulges is created on a tough hydrogel film by DLP printing. This film is further sandwiched by a pair of carbon fabric sheets to devise a capacitive pressure sensor (Fig. 7e). The presence of hollow pyramid-like bulges affords the sensor with a high sensitivity (2.6 kPa^{-1}) to applied pressure. This pressure sensor can be used to monitor the pressure variation on the surface of the device when a water drop is dripped on. As shown in Fig. 7f, this device exhibits high sensitivity and stability to detect the impact of a water droplet falling from a height of 5 cm. Other tough hydrogels should be also processed by DLP printing technology given that dense associative interactions are quickly formed *in situ* as the physical crosslinks to immediately toughen the networks [90–94]. Engineering of tough hydrogels by 3D printing technologies opens opportunities of gel materials in diverse fields, especially when excellent mechanical properties and elaborate architectures are both required.

9. Hydroplastic foaming graphene frameworks for acoustic and conductive polymer composites

Graphene, with a 2D topology, has emerged as an advanced nanofiller to improve the electronic, mechanical and thermal properties of polymer composites [95–98]. Following the traditional mixing protocol, graphene has exhibited high efficiency in enhancing the functions over other nanofillers. However, due to the strong π-π interaction force between graphene sheets, sheet aggregation is unavoidable in polymers, hindering the theoretical properties of graphene-based composites. Recently, we have invented a hydroplastic foaming (HPF) method [99] to achieve the fabrication of graphene aerogel with precise regulation of nano-scale wall, which can effectively avoid the sheet stacking in composites. Based on this thought, two major advances [100,101] have been realized so far.

The first development is the fabrication of a cellular graphene acoustic absorber with ultra-high efficiency in acoustic absorption (Fig. 8) [101]. We revealed the embedding of ultrathin graphene drums into commercial polymer foams by HPF method can remarkably improve its average absorption efficient ~320% from 200 Hz to 6000 Hz. We demonstrated the graphene drum with ultrathin thickness serves as intrinsically resonant elements to dissipate sound transport by large out-of-plane resonance [102–104]. We found that the thinner graphene nanofilm exhibits stronger resonant effect by prototype test and theoretical modeling. Numerical results showed that the out-of-plane resonance amplitude increases monotonically as thickness decreases, indicating the high efficiency of ultrathin graphene drums introduced by HPF. We experimentally validated the graphene-based composite foam (PFGA) with a thickness of 30 mm exhibited a high absorption coefficient above 0.8–0.9 to cover a wide frequency range from 200 Hz to 6000 Hz, including the usual noise range, extending from

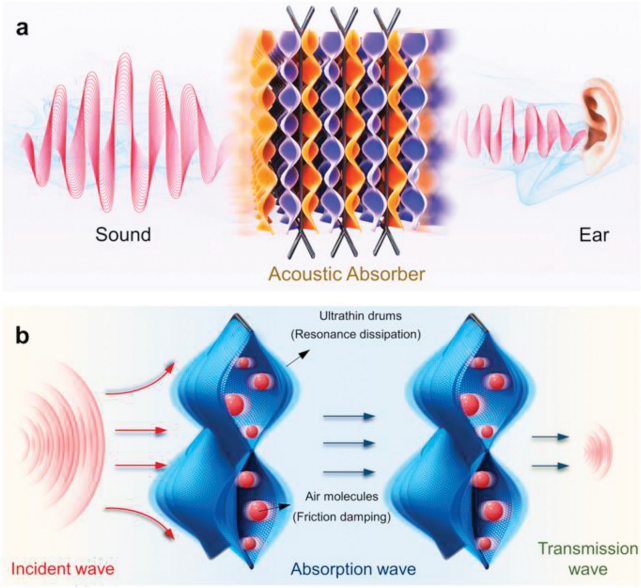

Fig. 8. (a) The proposed structure model of graphene-based, which includes the polymer porous motif and self-standing ultrathin graphene membranes. (b) The multiple mechanisms of the graphene-based absorber to achieve superior absorption by the resonance of ultrathin graphene and air friction damping in the pores. Reproduced with permission [101]. Copyright 2022, Wiley-VCH.

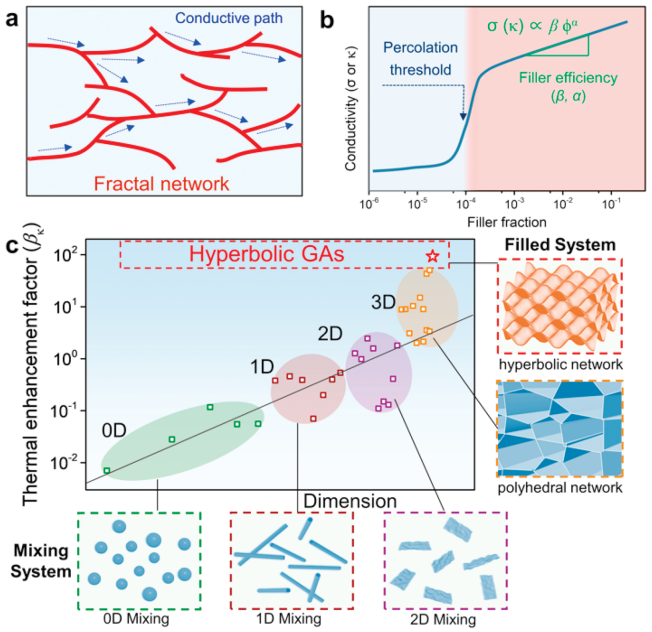

Fig. 9. Schematic illustrations of polymer nanocomposites with 0D, 1D, 2D, and 3D nanofillers. (a) Representative diagram of continuous conductive paths in a polymer nanocomposite and (b) its typical evolution of conductive performances. (c) Thermal enhancement factor of polymer nanocomposites with different nanofillers, divided into mixing and filled systems. Reproduced with permission [100]. Copyright 2022, American Chemical Society.

residential, vocal to traffic and industrial noises. Moreover, the specific noise reduction coefficient (NRC) and greater efficiency of PFGA surpassed most of the reported sound-absorption materials, such as the conventional porous materials, composites and ultralight aerogels, in which air friction mechanism dominates. We further proved the resonances of graphene drums mainly acted on low-frequency sound attenuation (200–1000 Hz) and the air-friction attenuation was the predominant mechanism at high-frequency of 4000–6000 Hz. The resonance and friction damping collectively work in the frequency from 1000 Hz to 4000 Hz. Integrating with prototype devices, we demonstrated the graphene absorber effectively attenuates the sound wave propagation in practical buzzer and audio environments. The graphene absorber provides an effective strategy to explore the superior resonance damping of 2D sheets, endows commercial foams with superior economic values, and satisfies the urgent demands for acoustic absorption from noise protection, instruments to building design, and acoustic devices.

Besides, the continuous GAs can prevent the sheets aggregation in composites and address the weak tunneling transport of a polymer gapped connection [105–108]. We demonstrated the hyperbolic graphene aerogels (HGAs) from HPF exhibited the positive Gaussian curvature, which can act as a geometrically optimal filler to fabricate highly conductive silicon rubber composites [100]. We measured the electrical conductivity (σ) and thermal conductivity (κ) of HGA composites (PGCs) with a series of containing and assessed the efficiency parameter (β) in the frame of the scaling relationship. The high efficiency in PGCs exceeds the efficiency previously achieved in functional nanocomposites of diversely topologic nanofillers, as shown in Fig. 9. The β_κ value of PGC (93) is nearly 2 orders of magnitude higher than that of the mixing composites, in which phonon transport is blocked by the gapped polymer between nanofillers. By comparison, the PGC has a breakthrough efficiency, achieving nearly 1 order of magnitude higher than that of nanocomposites with conventional polyhedral network. We verified the hyperbolic network forms face-to-face contact of 2D sheets and provided more conductive paths than that of the polyhedral network with the line-line contact configuration. Moreover, we developed the analytical formulas based on the two-dimensional representative volume element (RVE) model with unit depth to analyze the contact areas and conductivities of hyperbolic (HGAs) and polyhedral (FDGAs) structures. The superior efficiency originates from the hyperbolically curved conformations of graphene sheets with tight facial contact and broader conductive paths. The polymer composites with hyperbolic graphene networks exhibit high thermal (31.6 W m^{-1} K^{-1}) and electrical (13,911 S/m) conductivities at an exceptionally low volume fraction of only 1.6%. The hyperbolically curved graphene network is beneficial for the curvature design of 2D sheets and other fillers, provides an effective method to manipulate the 3D structure of functional composites, and can be extended to sensors and energy storage.

10. Aggregate photophysics of the through-space interactions

Clusteroluminescence (CL) is a photophysical phenomenon observed in non-conjugated molecules that exhibit unconventional luminescence in their clustering state [109]. In recent years, CL has garnered significant theoretical and practical interest. Traditional theories of through-bond conjugation are unable to explain this phenomenon, posing a challenge in the design of high-efficiency luminogens with CL (CLgens) [110]. Recent studies suggest that through-space interactions (TSIs) play a crucial role in CL [111], unlike in fused-ring luminophores where through-bond conjugation dominates. Intramolecular TSIs refer to the spatial electronic communication among different isolated units, inducing a narrow energy gap that corresponds to CL. However, establishing a clear structure-property relationship of TSIs remains a significant challenge, as it is a crucial aspect of aggregate photophysics construction [112].

To address the above-mentioned challenge, our group has focused on understanding the nature of through-space interactions (TSIs) and manipulating their strength in small molecules with non-conjugated structures. As shown in Fig. 10a, we designed and synthesized three triphenylmethane-based molecules with dif-

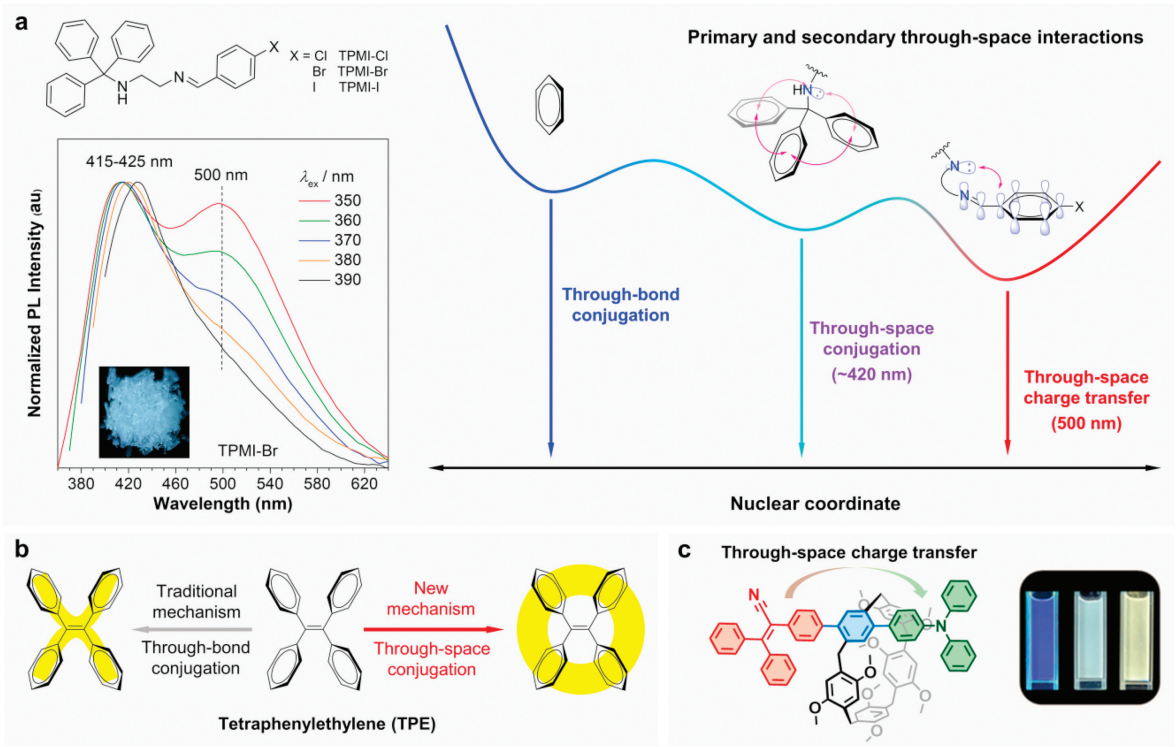

Fig. 10. (a) Multi-level through-space interactions in triphenylmethane-based clusteroluminogens. Reproduced with permission [113]. Copyright 2022, licensed under CC-BY. (b) Schematic illustration of the through-space conjugation in tetraphenylethylene. (c) Pillararene-induced intramolecular through-space charge transfer. Reproduced with permission [117]. Copyright 2022, Wiley-VCH.

ferent heteroatoms (TPMI-Cl, TPMI-Br, TPMI-I) [113]. Excitation-dependent photoluminescence (PL) spectra demonstrated that the crystal of TPMI-Br exhibits two emission peaks: short-wavelength emission around 420 nm and long-wavelength emission around 500 nm. The intensity ratio of these two peaks could be adjusted by the excitation wavelength. The crystal of TPMI-Br also shows white-light emission under 365 nm excitation. Furthermore, the long-wavelength emission is intensified as the heteroatom is switched from Cl to Br and I. Systematic experimental characterization and quantum-mechanical calculations revealed that the blue emission around 420 nm is induced by through-space conjugation (TSC) of triphenylmethane (TPM) [114], and the long-wavelength emission around 500 nm is derived from through-space charge transfer between the donor of TPM and acceptor of halogen-substituted phenylmethanimine. Based on these results, we have introduced the concept of primary and secondary through-space interactions, which not only reveal the nature of TSIs in CLgens but also provide an effective strategy for manipulating the CL performance through the heavy-atoms effect.

Building on the concept of TSIs in nonconjugated CLgens, we explored the luminescent properties of the traditional conjugated chromophores of tetraphenylethane (TPE), a widely-studied luminogen with aggregation-induced emission (AIE) effect [115]. Previous research attributed the blue emission of TPE around 460 nm to through-bond conjugation among four phenyl rings across the central double bond (Fig. 10b, left). However, our systematic theoretical calculations revealed that the middle double bond was elongated and broken in the excited state, becoming a quasi-double bond, which is not a typical π-conjugated structure [116]. The true emissive species is the through-space conjugation among four phenyl rings (Fig. 10b, right). We found that TSC is a widely-present interaction in twisted structures, regardless of whether they are conjugated or nonconjugated molecules. With this in mind, we designed a donor (D)-acceptor (A) molecule with two D/A moieties connected by a macrocycle of pillararene (Fig. 10c) [117]. The crystal structure revealed that the D and A parts were almost entirely separated due to the strong steric hindrance caused by the pillararene. Interestingly, the separated D/A structures exhibited two emission peaks in the aggregate state: a short one around 420 nm from the isolated D/A units and a long-wavelength emission around 530 nm corresponding to the through-space charge transfer between the D-A units. This finding provides a novel strategy for designing D/A-based chromophores. Additionally, the pillararene-based D/A structures displayed responsiveness to viscosity and polar guests. The theory of TSIs promises to bring about a paradigm shift in photophysics, moving from molecular to aggregate systems and from conjugated luminophores to CLgens. The development of TSIs theories will advance the practical application of CLgens as a novel luminescent material.

11. The nested texture in poly(L-lactic acid) (PLLA) spherulitic films

Polymorphism, which exists widely in semi-crystalline polymers, significantly influence the thermal [118], permeable [119], mechanical [120] or optical [121] properties of polymer materials. Recently, we have observed a nested spherulitic texture (Fig. 11a) [122] in spin-coated PLLA, a promising biodegradable [123] and biocompatible [124–127] material, after isothermal crystallization. In such PLLA films, a small α' spherulite nests in the center of a large α spherulite, as evidenced by that the two spherulites exhibit different cross-extinction as well as disparate Raman signals. More importantly, within a textured film, the two forms of PLLA spherulites show significant difference in degradation, indicating that it may possible to balance the degradation and mechanical

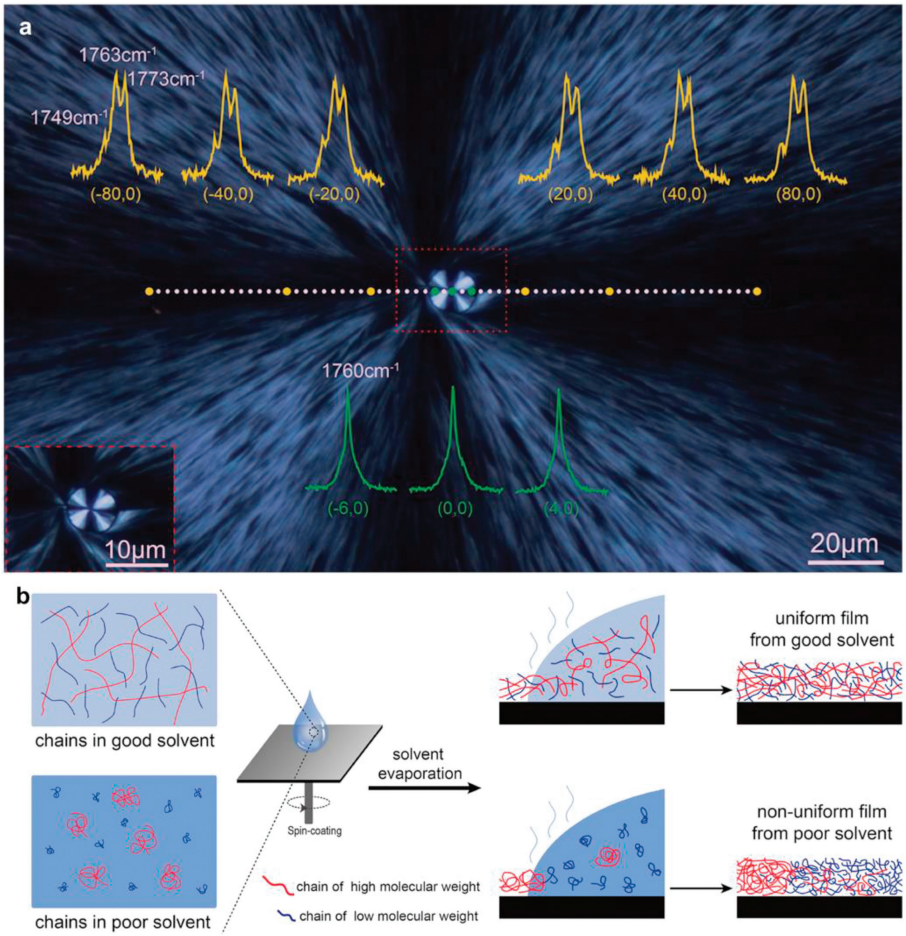

Fig. 11. (a) A polarizing optical microscopy (POM) image of the nested spherulites of PLLA obtained from isothermal crystallization. (b) Schematics illustrating the states of PLLA chains in good and poor solvents, and different distributions of chains with different molecular weights in films after spin coating. Reproduced with permission [128]. Copyright 2022, American Chemical Society.

properties of a PLLA-based materials by tailoring the spherulitic morphology.

On this basis, we investigated the forming mechanism, as well as the influencing factors, of the nested texture [128]. Generally, the isothermal nucleation of the nested α' spherulite is caused by the pre-sediment of high molecular weight (MW) PLLA chains during spin-coating. After melting the dried films followed by isothermal crystallization, these localized aggregations of high MW chains tend to nucleate as α' form. Consequently, higher MW and larger polydispersity of PLLA can promote the fractional precipitation and, in a result, facilitate the occurrence of the nested and polymorphic texture. Furthermore, chain conformation in solutions play a crucial role in guiding the localized aggregation of high MW chains. In poor solvents, PLLA chains tend to collapse and separate, leading to easier pre-sediment of high MW chains. Otherwise, in good solvents, the entanglements of PLLA chains with different MW bring difficulties in chain separation and hence the localization of high MW chains aggregation becomes harder (Fig. 11b). Therefore, weak solubility and low temperature of the solvent are critical factors to the formation of the nested morphology, as well. By simply altering the composition or temperature of the solvents, it is able to control the texture morphologies. Considering the universality of the polydispersity in polymers, the fractional precipitation during film fabrication might be one of the reasons for polymorphism formation. More importantly, this work provides a novel strategy to modulate the properties of polymer materials by tailoring the polymorphic texture [129].

12. The isotropically dyeing process of single crystals grown from hydrogels

A transparent single crystal can incorporate chromophores or luminophores inside, forming dye inclusion crystal (DIC) [130]. This unusual structure provides a platform to investigate the crystallization mechanism [131]. Moreover, the dye-incorporation is able to enhance the optical, thermal or mechanical properties of the host single crystals, which is significant for the non-linear optical (NLO) crystal martials [132] or other optical materials. In the related reports, for instance, dye-doped NLO crystals exhibit improved transmittance [133] and second harmonic generation efficiency [134], reinforced hardness [135], increased laser damage threshold [136], as well as enhanced thermal stability [137].

Conventionally, potassium dihydrogen phosphate (KDP) single crystal, a typical NLO material [138–140], which grows within methylene blue (MLB) (Fig. 12a) or aniline blue (ALB) (Fig. 12b) aqueous solution can only be stained anisotropically. This is given by the specific electrostatic interaction between ionic dye molecules and certain crystal facets, and hence the incorporation of dyes into specific region of a crystal. However, the non-uniformity limits the optical application of such dyed NLO crystals. Therefore, we used silica hydrogels, which contain MLB or ALB, as growing media of KDP single crystals [141]. Interestingly, these gel-grown crystals were stained isotropically with dyes being occluded along with gel-networks (Fig. 12c for MLB and Fig. 12d for ALB), while maintain their single-crystallinity. Moreover, we found an

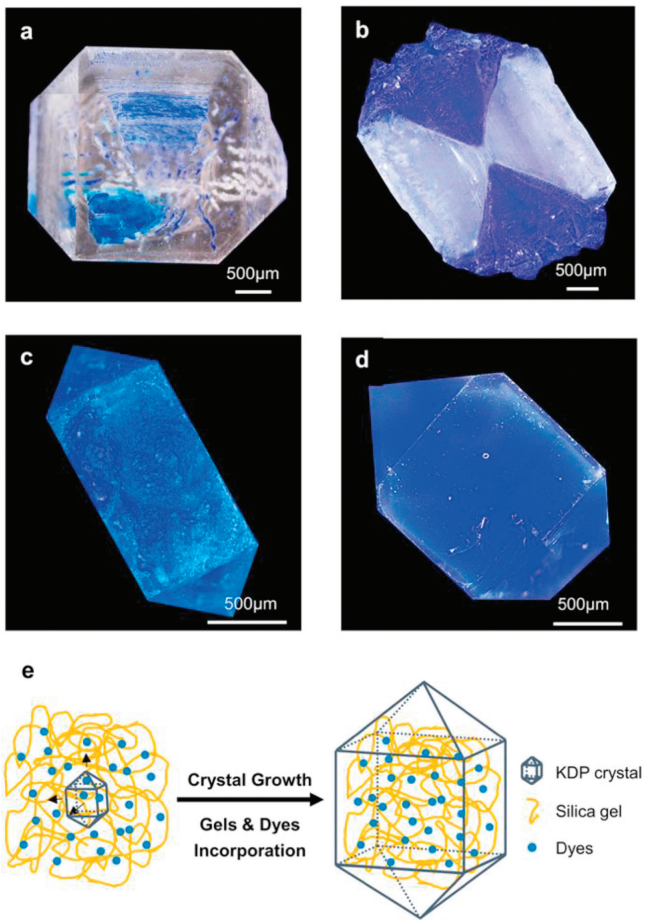

Fig. 12. OM images of KDP crystals grown from solution (a, b) or silica gels (c, d) with MLB (a, c) or ALB (b, d) molecules incorporated inside. (e) Schematic representation of KDP crystallization in silica gels containing dyes. Reproduced with permission [141]. Copyright 2022, American Chemical Society.

enrichment of ALB from gel media into gel-grown KDP single crystals, where the content of dyes was much higher than that in the original gels. This was given by the strong binding interaction between ALB molecules and gel-networks, and consequently the accumulation of ALB onto the gel-networks.

As we demonstrated the accommodation of dye molecules along gel-networks by investigating the shortened PL lifetimes of the dyes in gels, the dyeing mechanism of KDP in the presence of silica gels, which is different with that of KDP stained in solutions, can be deduced. First, dyes bind to the gel-networks owing to their attraction such as H-bond. Second, the interconnected gel-networks withstand the advancing fronts of growing crystals and hence physically bind to all the growing surfaces, leading to their isotropic occlusion by growing crystals. In a result, the dyes carried by gel-networks are uniformly incorporated into KDP single crystals (Fig. 12e). This work provides a novel bio-inspired strategy for the synthesis of versatile DIC materials.

13. Conclusion

In conclusion, we briefly review the breakthroughs made by the laboratory in eleven research directions in 2022. The first is the developments and catalytic performances of dinuclear organoboron catalysts. The second is polyester synthesis through cationic copolymerization of cyclic anhydride. The third is ring-opening polymerization of carbon dioxide based valerolactone. The fourth is improvements of machine learning-assisted biomaterial research. The fifth is development of methods for characterization of biomacromolecule RNA transcription and manipulation of nucleoside modification. The sixth is the establishment of artificial enzymes-armed *Bifidobacterium Longum* probiotics to tune down gut inflammation. The seventh is the processing of tough supramolecular hydrogels by 3D printing technologies. The eighth is the research of hydroplastic foaming graphene frameworks for acoustic and conductive polymer composites. The ninth is breakthrough of aggregate photophysics of the through-space interactions. The tenth is the forming mechanism of a newfound nested texture in PLLA spherulitic films. The final is the isotropically dyeing mechanism of KDP single crystals grown from hydrogels. We believe that these excellent accomplishments and scientific viewpoints will provide great prospects in promoting the preparation, mechanism research and practical application of versatile functional polymer materials.

Declaration of competing interest

The authors declare that they have no known competing financial interests or personal relationships that could have appeared to influence the work reported in this paper.

Acknowledgment

The authors acknowledge the support from the SCI-TECH Academy of Zhejiang University.

References

[1] J. Ren, X. Shu, Y. Wang, et al., Chin. Chem. Lett. 33 (2022) 1650–1658.
[2] Q. Wen, Q. Cai, P. Fu, et al., Chin. Chem. Lett. 34 (2023) 107592.
[3] Y. Zhu, C. Romain, C.K. Williams, Nature 540 (2016) 354–362.
[4] D.J. Darensbourg, Chem. Rev. 107 (2007) 2388–2410.
[5] X.B. Lu, D.J. Darensbourg, Chem. Soc. Rev. 41 (2012) 1462–1484.
[6] C.A.L. Lidston, S.M. Severson, B.A. Abel, G.W. Coates, ACS Catal. 12 (2022) 11037–11070.
[7] G.W. Yang, C.K. Xu, R. Xie, et al., Nat. Synth. 1 (2022) 892–901.
[8] Y.Y. Zhang, G.W. Yang, R. Xie, X.F. Zhu, G.P. Wu, J. Am. Chem. Soc. 144 (2022) 19896–19909.
[9] Y.Y. Zhang, C. Lu, G.W. Yang, et al., Macromolecules 55 (2022) 6443–6452.
[10] H. Qi, R. Xie, G.W. Yang, et al., Macromolecules 55 (2022) 9081–9090.
[11] G.W. Yang, Y. Wang, H. Qi, et al., Angew. Chem. Int. Ed. 61 (2022) e202210243.
[12] Y. Yan, G. Wu, S. Chen, Y. Wang, Chin. Chem. Lett. 33 (2022) 2151–2154.
[13] S. Hu, J. Zhao, G. Zhang, H. Schlaad, Prog. Polym. Sci. 74 (2017) 34–77.
[14] X. Zhou, Q. Liu, G. Xu, et al., Chin. Chem. Lett. 34 (2023) 108158.
[15] C. Zhang, X. Zhang, X. Zhang, Sci. China Chem. 63 (2020) 1807–1814.
[16] X. Cao, H. Wang, J. Yang, et al., Chin. Chem. Lett. 33 (2022) 1021–1024.
[17] Y. Wang, J.L. Yang, C.J. Zhang, X.H. Zhang, Acta Polym. Sin. 51 (2020) 1092–1103.
[18] J.M. Longo, M.J. Sanford, G.W. Coates, Chem. Rev. 116 (2016) 15167–15197.
[19] C. Zhang, X. Geng, X. Zhang, Y. Gnanou, X. Feng, Prog. Polym. Sci. 136 (2023) 101644.
[20] L. Hu, C. Zhang, D. Chen, et al., ACS Appl. Polym. Mater. 2 (2020) 5817–5823.
[21] X. Zhang, C. Zhang, X. Zhang, Angew. Chem. Int. Ed. 61 (2022) e202117316.
[22] X. Zhang, Y. Sun, C. Zhang, X. Zhang, CCS Chem. 5 (2023) 1233–1241.
[23] A. Birke, J. Ling, M. Barz, Prog. Polym. Sci. 81 (2018) 163–208.
[24] C. Zhuo, H. Cao, X. Wang, S. Liu, X. Wang, Chin. Chem. Lett. 34 (2023) 108011.
[25] H. Luo, J. Ren, Y. Sun, et al., Chin. Chem. Lett. 34 (2023) 107782.
[26] J. Zhou, H. Liu, H. Wang, Chin. Chem. Lett. 34 (2023) 107420.
[27] C.J. Price, B.J.E. Reich, S.A. Miller, Macromolecules 39 (2006) 2751–2756.
[28] R. Nakano, S. Ito, K. Nozaki, Nat. Chem. 6 (2014) 325–331.
[29] A. Behr, G. Henze, Green Chem. 13 (2011) 25–39.
[30] S. Yue, T. Bai, S. Xu, et al., ACS Macro Lett. 10 (2021) 1055–1060.
[31] S. Tang, K. Nozaki, Acc. Chem. Res. 55 (2022) 1524–1532.
[32] K. Chen, Y. Mei, Z. Zhang, J. Ling, X. Ni, ChemPlusChem 88 (2023) e202300022.
[33] K. Chen, Z. Zhu, T. Bai, et al., Angew. Chem. Int. Ed. 134 (2022) e202213028.
[34] J. Song, K. Chen, Y. Feng, X. Ni, J. Ling, J. Polym. Sci. 60 (2022) 2352–2361.
[35] N. Fleming, Nature 557 (2018) S55–S57.
[36] J. Jumper, R. Evans, A. Pritzel, et al., Nature 596 (2021) 583–589.
[37] J. Zhang, J. Chen, P. Hu, H. Wang, Chin. Chem. Lett. 31 (2020) 890–896.
[38] M. Hussain, X. Liu, J. Zou, et al., Chin. Chem. Lett. 33 (2022) 1885–1888.
[39] K.T. Butler, D.W. Davies, H. Cartwright, O. Isayev, A. Walsh, Nature 559 (2018) 547–555.
[40] D. Reker, Y. Rybakova, A.R. Kirtane, et al., Nat. Nanotechnol. 16 (2021) 725–733.

[41] Y.F. Xue, Y. He, J. Wang, et al., Small Methods 6 (2022) e2101405.
[42] H. Hao, Y. Xue, Y. Wu, et al., Bioact. Mater. 28 (2023) 1–11.
[43] Y. Wei, Y. Ji, L.L. Xiao, et al., Biomaterials 34 (2013) 2588–2599.
[44] M. Muttenthaler, G.F. King, D.J. Adams, P.F. Alewood, Nat. Rev. Drug Discov. 20 (2021) 309–325.
[45] N. Mookherjee, M.A. Anderson, H.P. Haagsman, D.J. Davidson, Nat. Rev. Drug Discov. 19 (2020) 311–332.
[46] M. Kai, W. Zhang, H. Xie, et al., Chin. Chem. Lett. 29 (2018) 1163–1166.
[47] B.P. Lazzaro, M. Zasloff, J. Rolff, Science 368 (2020) eaau5480.
[48] J. Huang, Y. Xu, Y. Xue, et al., Nat. Biomed. Eng. 7 (2023) 797–810.
[49] S. Osman, P. Cramer, Annu. Rev. Cell Dev. Biol. 36 (2020) 1–34.
[50] J. Bassler, E. Hurt, Annu. Rev. Biochem. 88 (2019) 281–306.
[51] K.A. Tatosyan, I.G. Ustyantsev, D.A. Kramerov, Mol. Biol. 54 (2020) 542–561.
[52] E.M. Wissink, A. Vihervaara, N.D. Tippens, J.T. Lis, Nat. Rev. Genet. 20 (2019) 705–723.
[53] I.A. Roundtree, M.E. Evans, T. Pan, C. He, Cell 169 (2017) 1187–1200.
[54] H. Shi, J. Wei, C. He, Mol. Cell 74 (2019) 640–650.
[55] M. Gao, Y. Li, X. Shu, et al., ACS Chem. Biol. 17 (2022) 768–775.
[56] M. Gao, S. Su, J. Cao, et al., ACS Chem. Biol. 17 (2022) 854–863.
[57] X. Shu, Q. Dai, T. Wu, et al., J. Am. Chem. Soc. 139 (2017) 17213–17216.
[58] X. Shu, J. Cao, M. Cheng, et al., Nat. Chem. Biol. 16 (2020) 887–895.
[59] L.J. Core, J.J. Waterfall, J.T. Lis, Science 322 (2008) 1845–1848.
[60] T. Wu, R. Lyu, Q. You, C. He, Nat. Methods 17 (2020) 515–523.
[61] S. Citi, Science 359 (2018) 1097–1098.
[62] J.Lloyd Price, C. Arze, A.N. Ananthakrishnan, et al., Nature 569 (2019) 655–662.
[63] D.R. Plichta, D.B. Graham, S. Subramanian, R.J. Xavier, Cell 178 (2019) 1041–1056.
[64] M. Sun, W. Ban, H. Ling, et al., Chin. Chem. Lett. 33 (2022) 4449–4460.
[65] W. Hu, D. Gao, Z. Su, et al., Chin. Chem. Lett. 33 (2022) 2096–2100.
[66] J. Suez, N. Zmora, E. Segal, E. Elinav, Nat. Med. 25 (2019) 716–729.
[67] M.Z. Cader, A. Kaser, Nat. Med. 27 (2021) 1870–1871.
[68] A.L. Brioukhanov, A.I. Netrusov, Appl. Biochem. Microbiol. 43 (2007) 567–582.
[69] F. Cao, L. Jin, Y. Gao, et al., Nat. Nanotechnol. 18 (2023) 617–627.
[70] F. Cao, L. Zhang, Y. You, et al., Angew. Chem. Int. Ed. 59 (2020) 5108–5115.
[71] C. Zhang, Z. Yu, J. Zhao, et al., J. Funct. Foods 53 (2019) 157–165.
[72] H. Fan, J.P. Gong, Macromolecules 53 (2020) 2769–2782.
[73] X. Zhao, X. Chen, H. Yuk, et al., Chem. Rev. 121 (2021) 4309–4372.
[74] D. Jiao, Q.L. Zhu, C.Y. Li, Q. Zheng, Z.L. Wu, Acc. Chem. Res. 55 (2022) 1533–1545.
[75] H. Xu, Y. Liu, X.M. Xie, Chin. Chem. Lett. 34 (2023) 107470.
[76] P. Li, Y. Liu, Z. Wang, et al., Chin. Chem. Lett. 33 (2022) 871–876.
[77] H.J. Zhang, X. Wang, Y. Yang, et al., Macromolecules 55 (2022) 7401–7410.
[78] H. Xu, X.M. Xie, Chin. Chem. Lett. 32 (2021) 521–524.
[79] H. Ju, H. Zhang, L.X. Hou, et al., J. Am. Chem. Soc. 145 (2023) 3763–3773.
[80] P. Schaaf, J.B. Schlenoff, Adv. Mater. 27 (2015) 2420–2432.
[81] X. Dai, Y. Zhang, L. Gao, et al., Adv. Mater. 27 (2015) 3566–3571.
[82] A. Zhang, F. Wang, L. Chen, et al., Chin. Chem. Lett. 32 (2021) 2923–2932.
[83] X.N. Zhang, Q. Zheng, Z.L. Wu, Compos. Part B: Eng. 238 (2022) 109895.
[84] W. Li, M. Wang, L.S. Mille, et al., Adv. Mater. 33 (2021) e2102153.
[85] M. Dong, Y. Han, X.P. Hao, et al., Adv. Mater. 34 (2022) e2204333.
[86] H.C. Yu, X.P. Hao, C.W. Zhang, et al., Small 17 (2021) e2103836.
[87] H.C. Yu, S.Y. Zheng, L. Fang, et al., Adv. Mater. 32 (2020) e2005171.
[88] W. Cui, Y. Zheng, R. Zhu, et al., Adv. Funct. Mater. 32 (2022) 2204823.
[89] Y. Huang, S. Qian, J. Zhou, et al., Adv. Funct. Mater. 33 (2023) 2213549.
[90] X.P. Hao, C.W. Zhang, W. Hong, et al., Mater. Horiz. 10 (2023) 432–442.
[91] G. Huang, Z. Tang, S. Peng, et al., Macromolecules 55 (2021) 156–165.
[92] C.Y. Li, S.Y. Zheng, X.P. Hao, et al., Sci. Adv. 8 (2022) eabm9608.
[93] L. Zhang, H. Yan, J. Zhou, et al., Adv. Mater. 35 (2023) e2202193.
[94] M. Wang, P. Zhang, M. Shamsi, et al., Nat. Mater. 21 (2022) 359–365.
[95] X. Sun, C. Huang, L. Wang, et al., Adv. Mater. 33 (2021) e2001105.
[96] X. Huang, C. Zhi, Y. Lin, et al., Mater. Sci. Eng. R 142 (2020) 100577.
[97] X. Huang, X. Qi, F. Boey, H. Zhang, Chem. Soc. Rev. 41 (2012) 666–686.
[98] T. Kuilla, S. Bhadra, D. Yao, et al., Prog. Polym. Sci. 35 (2010) 1350–1375.
[99] K. Pang, X. Song, Z. Xu, et al., Sci. Adv. 6 (2020) eabd4045.
[100] X. Liu, K. Pang, H. Qin, et al., ACS Nano 16 (2022) 14703–14712.
[101] K. Pang, X. Liu, J. Pang, et al., Adv. Mater. 34 (2022) e2103740.
[102] R. De Alba, F. Massel, I.R. Storch, et al., Nat. Nanotech. 11 (2016) 741–746.
[103] R.A. Barton, B. Ilic, A.M. van der Zande, et al., Nano Lett. 11 (2011) 1232–1236.
[104] A. Blaikie, D. Miller, B.J. Aleman, Nat. Commun. 10 (2019) 4726.
[105] X. Shen, Z. Wang, Y. Wu, et al., Mater. Horiz. 5 (2018) 275–284.
[106] J. Yang, X. Li, S. Han, et al., J. Mater. Chem. A 6 (2018) 5880–5886.
[107] J. Yang, G.Q. Qi, Y. Liu, et al., Carbon 100 (2016) 693–702.
[108] Y. Li, W. Wei, Y. Wang, et al., J. Mater. Chem. C 7 (2019) 11783–11789.
[109] B. Liu, B. Chu, L. Zhu, et al., Chin. Chem. Lett. 34 (2023) 107909.
[110] H. Zhang, Z. Zhao, P.R. McGonigal, et al., Mater. Today 32 (2020) 275–292.
[111] H. Zhang, B.Z. Tang, JACS Au 1 (2021) 1805–1814.
[112] H. Zhang, Z. Zhao, A.T. Turley, et al., Adv. Mater. 32 (2020) e2001457.
[113] J. Zhang, P. Alam, S. Zhang, et al., Nat. Commun. 13 (2022) 3492.
[114] J. Zhang, L. Hu, K. Zhang, et al., J. Am. Chem. Soc. 143 (2021) 9565–9574.
[115] J. Zhang, H. Zhang, J.W.Y. Lam, B.Z. Tang, Chem. Res. Chin. Univ. 37 (2021) 1–15.
[116] J. Liu, H. Zhang, L. Hu, et al., J. Am. Chem. Soc. 144 (2022) 7901–7910.
[117] Q. Li, Y. Wu, J. Cao, et al., Angew. Chem. Int. Ed. 61 (2022) e202202381.
[118] M.L. Di Lorenzo, M.C. Righetti, B. Wunderlich, Macromolecules 42 (2009) 9312–9320.
[119] G. Liu, X. Zhang, D. Wang, Adv. Mater. 26 (2014) 6905–6911.
[120] C. De Rosa, M. Scoti, R. Di Girolamo, et al., Polym. Cryst. 3 (2020) e10101.
[121] M. Cocca, R. Androsch, M.C. Righetti, M. Malinconico, M.L. Di Lorenzo, J. Mol. Struct. 1078 (2014) 114–132.
[122] D. Hu, M. Chen, Y. Yang, H. Li, Chin. J. Polym. Sci. 38 (2020) 1365–1373.
[123] X. Hu, W. Zhao, Z. Zhang, et al., Chin. Chem. Lett. 34 (2023) 107451.
[124] Q. Gao, L. Duan, X. Feng, W. Xu, Chin. Chem. Lett. 32 (2021) 577–582.
[125] X. Li, X. Shu, Y. Shi, H. Li, X. Pei, Chin. Chem. Lett. 34 (2023) 107986.
[126] F. Xue, J.J.L.M. Cornelissen, Q. Yuan, S. Cao, Chin. Chem. Lett. 34 (2023) 107448.
[127] K. Huang, J. Huang, J. Zhao, Z. Gu, J. Wu, Chin. Chem. Lett. 33 (2022) 1941–1945.
[128] D. Hu, M. Chen, S. Lu, H. Li, Macromolecules 55 (2022) 8195–8202.
[129] X. Li, S. Semin, L.A. Estrada, et al., Chin. Chem. Lett. 29 (2018) 297–300.
[130] B. Kahr, R.W. Gurney, Chem. Rev. 101 (2001) 893–951.
[131] B. Kahr, T. Bullard, M. Kurimoto, J.J. De Yoreo, Cryst. Res. Technol. 48 (2013) 849–863.
[132] W. Wang, D. Mei, S. Wen, J. Wang, Y. Wu, Chin. Chem. Lett. 33 (2022) 2301–2315.
[133] S. Kumar, N. Sinha, S. Goel, B. Kumar, Vacuum 175 (2020) 109240.
[134] G. Durgababu, G.J. Nagaraju, G. Bhagavannarayana, J. Mater. Sci. Mater. Electron. 32 (2021) 2564–2578.
[135] S. Arumugam, S.J.D. Sathiyadhas, J. Michael, et al., J. Cryst. Growth 523 (2019) 125154.
[136] D. Kanimozhi, S. Nandhini, R. Indirajith, J. Mater. Sci Mater. El. 30 (2019) 10244–10255.
[137] N. Sinha, K. Batra, S. Bhukkal, et al., Arab. J. Chem. 13 (2020) 5750–5764.
[138] S. Liu, L. He, Y. Wang, P. Shi, Q. Ye, Chin. Chem. Lett. 33 (2022) 1032–1036.
[139] M. Yang, H. Cheng, Y. Xu, M. Li, Y. Ai, Chin. Chem. Lett. 33 (2022) 2143–2146.
[140] H. Chen, M.Y. Ran, S.H. Zhou, et al., Chin. Chem. Lett. 34 (2023) 107838.
[141] F. Gao, J. Ren, X. Jin, X. Deng, H. Li, ACS Mater. Lett. 4 (2022) 1207–1213.